Journal of Biomedical Optics 13(4), 044033 (July/August 2008)

Magnetic resonance imaging guidance for laser photothermal therapy

Yichao Chen
University of Central Oklahoma
College of Mathematics and Science
Department of Engineering and Physics
100 North University Drive
Edmond, OK 73034

Surya C. Gnyawali
Oklahoma State University
Department of Physics
Stillwater, Oklahoma 73019

Feng Wu
Chongqing Medical University
Institute of Ultrasonic Engineering in Medicine and
Clinical Center for Tumor Therapy of 2nd Affiliated Hospital
Medical College Road
Chongquing 400016, China

Hong Liu
University of Oklahoma
School of Computer Electrical Engineering and
Center for Bioengineering
Norman, Oklahoma 73019

Yasvir A. Tesiram
Andrew Abbott
Rheal A. Towner
Oklahoma Medical Research Foundation
825 N.E. 13th Street
Oklahoma City, Oklahoma 73104

Wei R. Chen
University of Central Oklahoma
College of Mathematics and Science
Department of Engineering and Physics
100 North University Drive
Edmond, OK 73034

Abstract. Temperature distribution is a crucial factor in determining the outcome of laser phototherapy in cancer treatment. Magnetic resonance imaging (MRI) is an ideal method for 3-D noninvasive temperature measurement. A 7.1-T MRI was used to determine laser-induced high thermal gradient temperature distribution of target tissue with high spatial resolution. Using a proton density phase shift method, thermal mapping is validated for *in vivo* thermal measurement with light-absorbing enhancement dye. Tissue-simulating phantom gels, biological tissues, and tumor-bearing animals were used in the experiments. An 805-nm laser was used to irradiate the samples, with laser power in the range of 1 to 3 W. A clear temperature distribution matrix within the target and surrounding tissue was obtained with a specially developed processing algorithm. The temperature mapping showed that the selective laser photothermal effect could result in temperature elevation in a range of 10 to 45°C. The temperature resolution of the measurement was about 0.37°C with 0.4-mm spatial resolution. The results of this study provide *in vivo* thermal information and future reference for optimizing laser dosage and dye concentration in cancer treatment. [DOI: 10.1117/1.2960020]

Keywords: laser phototherapy; selective photothermal interaction; magnetic resonance imaging (MRI); noninvasive temperature measurement; Indocyanine Green (ICG).

Paper 07411RR received Oct. 2, 2007; revised manuscript received Feb. 1, 2008; accepted for publication Mar. 12, 2008; published online Jul. 24, 2008.

1 Introduction

Photothermal interaction has been widely used in immunological stimulation[1] and treatment of tumors,[2] thermosensitive microcarries,[3] and heart arrhythmias.[4] *In vivo* temperature distribution mapping has clinical significance since the body temperature is closely related to physiological functions. Noninvasive temperature monitoring during hyperthermia,[5] nonincision surgery using ultrasound,[6] and laser immunotherapy[1,7–9] are critical and highly desirable for confirming the target region as well as determining treatment parameters. Specifically, real-time *in vivo* thermometry during photothermal treatment can improve the treatment effect by monitoring and optimizing the heat distribution generated by laser irradiation.

Thermal distribution induced by laser radiation is determined by both laser and tissue parameters.[10] Selective photothermal interaction, using *in situ* dye enhancement, can destroy tumor cells directly by raising target tissue temperature above the damage threshold using laser radiation. It could also

Address all correspondence to: Wei R. Chen, Ph.D. Professor, Department of Engineering and Physics College of Mathematics and Science, University of Central Oklahoma, 100 N. University Drive Edmond, Oklahoma 73034. Tel: (405) 974-5198; Fax: (405) 974-3812; E-mail: wchen@ucok.edu.

1083-3668/2008/13(4)/044033/8/$25.00 © 2008 SPIE

be used as an adjuvant to immunotherapy by exposing tumor antigens when combined with active immunological stimulation. Due to unknown differences in thermal conductivity, diffusion, and physiological cooling effects, the hyperthermic efficiency is hard to determine. The optimum outcome of the laser photothermal interaction is to kill as many target tumor cells as possible, while preserving tumor proteins for recognition of the host immune system. In order to achieve such effects while avoiding undesirable thermal damage to surrounding healthly tissue, the rise in temperature in target regions needs to be tightly controlled. The treatment effect has a close relationship with the thermal distribution inside the target tumor and surrounding tissue.

Magnetic resonance imaging (MRI) is ideal for noninvasive, real-time, 3-D temperature mapping and target visualization. Unlike many other thermal measurement modalities, MRI can determine temperature distribution in tissue without disturbing treatment procedures. There are several MRI measurement methods for temperature profiling.[11] The water proton resonance frequency shift (PRF) method is now the most promising method for thermology with high spatial resolution and fast data acquisition.[12–14] In the PRF method, temperature dependence comes from weak local magnetic field shielding caused by the moving electron clouds around the proton. When temperature increases, the screening effect of bounded electrons increases, resulting in a lower local magnetic field and consequently a negative shift of water PRF. A simple gradient echo sequence can be deployed, and the calibration curve is not needed because each tissue contains water molecules. The PRF method has been shown to be the most accurate method in the case of low motion state. There are several reports on PRF using materials such as optical tissue-like phantoms and tissue *in vitro*.[12,15] Optical tissue-simulating phantom gels such as agarose gels have been used in the thermal MRI measurement.[16] For the live animal model, this method has the challenge of decreasing the movement error because of phase subtraction. Respiratory gating is needed with anesthetized animals.

In this study, the PRF method was used for the 3-D temperature mapping under laser irradiation using a 7-T small animal MR scanner. The high magnetic field can lead to high sensitivity and fine resolution, which are crucial in point-like thermal distribution during laser irradiation. The temperature distributions were measured using *in vivo* and *ex vivo* tissues, phantom gels, and live animals. A phantom gel with tissue-like optical properties has not been previously used for such applications. The temperature increase of various samples were measured by MRI and calibrated by thermocouples and fiber temperature sensor systems. The influence of external magnetic field fluctuation and system noise was investigated. The current study could lead to better understanding of the relationship between the tissue parameters and laser parameters in photothermal therapy. It may also provide a fundamental framework for understanding the immunological responses induced by phototherapy, since temperature has been related to the activation and enhancement of immune responses.

2 Materials and Methods

2.1 *Physical Basis*

The PRF method was first investigated by Hindman[17] in his study of hydrogen bond formation between water molecules. The magnetic field experienced by a proton within tissue, B_{local}, has the following relationship with the main external magnetic field, B_0,[17,18] which has the same unit of tesla:

$$B_{\text{local}} = [1 + \sigma(\text{T})]B_{0,}, \tag{1}$$

where $\sigma(T)$, the chemical shift, is the screening factor and is unitless.

When temperature increases, the screening factor decreases, causing decrease of B_{local}.

Using the assumption of linear temperature dependence of $\sigma(T)$, this can lead to:[12]

$$\Delta\sigma(\text{T}) = \alpha\Delta\text{T}, \tag{2}$$

where α is the temperature-dependent water proton chemical shift in ppm/°C and ΔT is the temperature change in Celsius.

With a certain phase image as a reference, one can acquire the temperature changes between two acquisition intervals:[19]

$$\Delta\varphi = \text{TE}\gamma\Delta\text{B}_{\text{local}} = \text{TE}\gamma\text{B}_0\alpha\Delta\text{T}, \tag{3}$$

where γ is the gyromagnetic ratio of hydrogen ($\gamma = 2\pi \cdot 42.57$ MHz/T), and TE is the echo time of the gradient echo pulse sequence with a unit of sec. Within physiological temperature ranges, α can be considered a constant.[12,20] Therefore, the temperature change is proportional to the phase change of the image at each corresponding pixel.

2.2 *Experiment Setup*

All experiments were carried out on a 7.1-T Bruker 730 USR 30-cm horizontal-bore small animal MR imaging system, controlled by ParaVision 3.0.2 software (Bruker BioSpin MRI GmbH, Germany).

An 805-nm laser was used in our experiments, and the delivery system is shown in Fig. 1. The laser power was delivered through a 7-m microlens fiber (Pioneer Optics, Windsor Locks, Connecticut) to the sample. The fiber contains a 400-μm core, with an output spot of 57-mm-diam at 100 mm with a half-angle divergence of 15.9 deg. A series of tests were performed using phantom gel, chicken tissue, and rat tumors. The laser power was chosen in a range of 1.0 to 3.0 W, according to the treated samples. The phantom gel was irradiated with a laser power density of 1.27 W/cm^2 (beam diameter of 1.0 cm and laser power of 1.0 W). The chicken breast was irradiated by laser with a power density of 1.17 W/cm^2 (beam diameter of 1.8 cm and laser power of 3 W), and tumor-bearing rats were treated with a power density of 2.55 W/cm^2 (beam diameter of 1.0 cm and laser power of 2.0 W). The laser irradiation duration was 10 min.

A chemical shift based on water proton density resonance frequency was used for temperature mapping. The typical MRI parameters used in our experiments were: $TE = 10$ ms and $TR = 158$ ms. The field of view (FOV) was 5.5 cm $\times$ 5.5 cm, with a slice thickness of 2.0 mm. The MRI temperature mapping image dimensions for the phantom gels

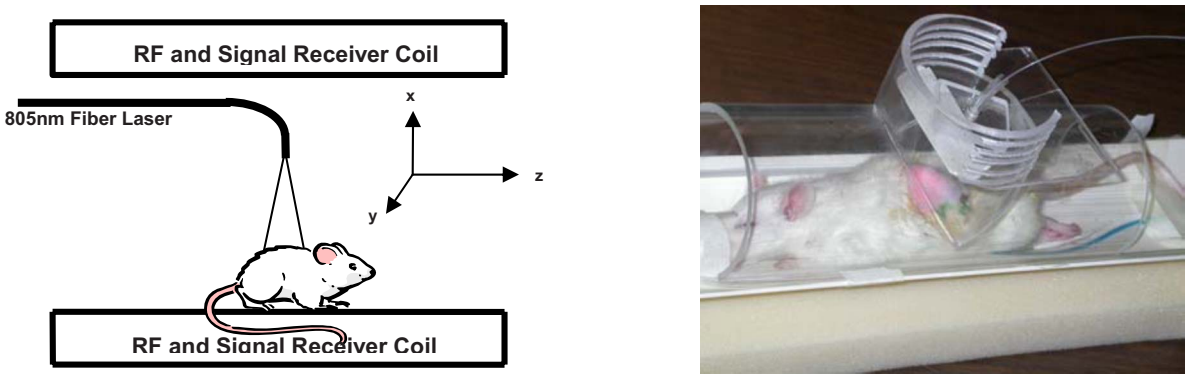

Fig. 1 Experimental setup. (a) Schematic of an animal inside the bore of an MR imager under laser irradiation. (b) Photo of the animal on a plastic holder before being placed in the MRI chamber. The optical fiber delivers the 805-nm laser light with suitable power density.

were 128×128 pixels, while the rat thermal distribution image dimensions were 256×256 pixels. The typical flip angle was 30 deg.

2.3 *Sample Preparation*

The tissue-simulating phantom gel consisted of gelatin and Liposyn (76% water, 20% Liposyn, and 4% gelatin). The gelatin gel was put in a cylinder container with a diameter of 5 cm and a height of 2.0 to 2.5 cm. One 0.5-cm-radius phantom gel sphere with 0.25% Indocyanine Green (ICG) (Akorn, Inc., Buffalo Grove, Illinois) was embedded in the gel 2 mm beneath the surface to simulate an absorption-enhanced tumor with a higher light absorption coefficient compared with that of the surrounding phantom gel.

Uncooked chicken breast tissue without bone was used. The chicken skin was removed. ICC solution (0.25%, 1 ml) was injected 30 min before MRI measurement.

The metastatic breast tumor strain DMBA-4 in female Wistar Furth rats was used in MRI measurement. A total of 10^5 viable tumor cells were injected subcutaneuosly on the back of the animal. The treatment took place when the primary tumor reached a size of 0.2 to 0.5 cm^3. Before treatment, the animal hair overlying the tumor was removed. Animals were anesthetized using a CDS 2000 portable anesthesia machine with flowmeter (SurgiVet, V700000MRI) with 2 to 2.5% Isoflurane at 2 to 2.5 L/min oxygen. Animals were constantly monitored using visual signs of respiration. ICG was injected 30 min before treatment. The animal protocol for this study was approved by the Institutional Animal Care and Use Committee of the Oklahoma Medical Research Foundation (OMRF).

2.4 *MRI Phase Mapping Signal Processing*

The MRI data was obtained using a fast low-angle shot (FLASH) MRI sequence. The real and imaginary data were collected and reconstructed from raw MRI data by MR image processing. The gradient echo MRI data were acquired during the experiments. The real and imaginary MRI data were used to extract the phase information using the arctangent of the ratio of the imaginary and real parts of the MRI data. The algorithm was implemented by Mathmatica. The phase differences were calculated by subtracting the reference phase image pixel by pixel from all of the subsequent phase images acquired during the experiments. The magnitude signal of a certain image was used as a filter with a certain threshold set in the algorithm to eliminate the noise points outside the gel region. The temperature change was obtained from the phase information. The MRI parameters such as *TE*, *TR*, and flip-angle were optimized to have a high signal-to-noise ratio, a low phase image noise, and short data acquisition time. The temperature information was exported to a Microsoft Excel file for pixel-to-pixel analyses and comparison. For each experiment, the laser treatment duration was 10 min. A 5-min background MRI measurement was taken before the laser irradiation, and a 15-min MRI measurement was taken after the laser irradiation for the thermal relaxation of the treated samples.

The phase information corresponding to the temperature changes was related to the reference point and the proton resonance shift coefficient. Normally, the phase information of the first image was used as a reference image. The temperature dependence of the water proton resonance frequency was about 0.01 ppm/°C,[21] which was nearly independent of the tissue composition.[22]

2.5 *System Evaluation*

In order to determine the system factor, a series of calibration tests was performed using different materials. The gels and chicken tissue were placed in a refrigerator with a thermometer to record the initial temperature. The samples were taken out of the refrigerator and placed in the bore of the magnet with a storage temperature of 5°C at the beginning of the MRI measurement. The sample temperature increased under laser radiation with the room temperature maintained at 22°C. The same procedure was repeated and the temperature measured using thermocouples. The two sets of data were compared with the same initial conditions to obtain the coefficient of thermal dependence for the water proton chemical shift.

The main system error of PRF measurement was contributed primarily by B_0 drift, vibrations, and rat breathing. According to Eq. (3), fluctuation on the order of 10^{-8} of the external magnetic field of B_0 would correspond to 1°C temperature change. Respiratory gating was used to eliminate any

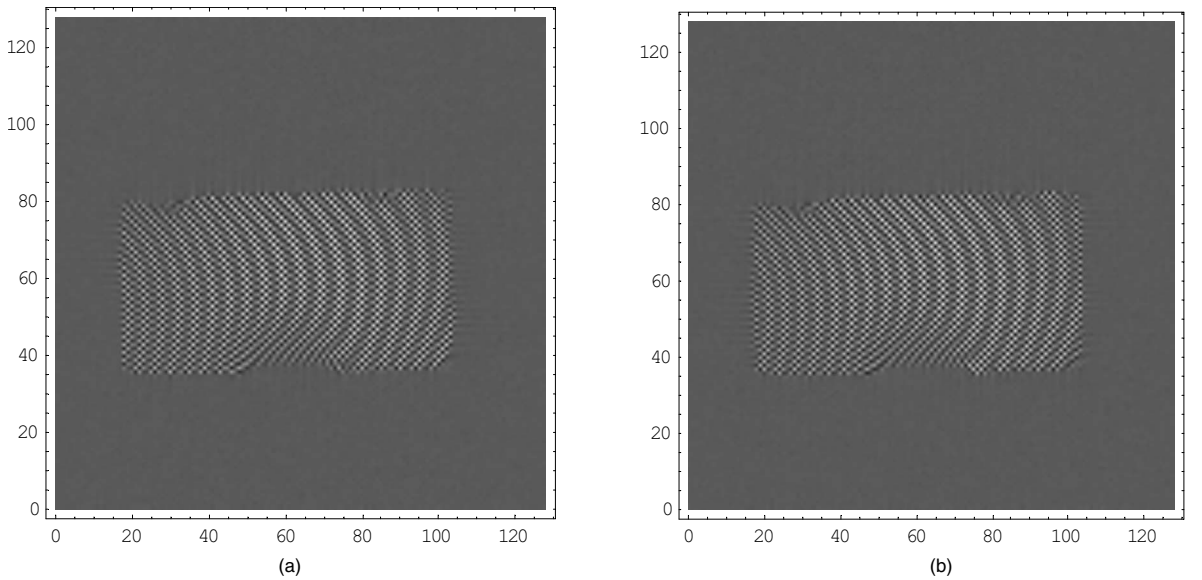

Fig. 2 Real (a) and imaginary (b) parts of the phantom gel data during laser irradiation after data reconstruction of an MRI image. The laser power density is 1.27 W/cm^2 with a laser power of 1.0 W. There is a phantom sphere (near the bottom of the sample) containing ICG (0.25%) embedded within the phantom gel to simulate the absorption-enhanced tumor.

motion artifacts caused by breathing.[23,24] Temporal resolution experiments were performed to evaluate the B_0 drift, as well as any other contributions from system error. This involved allowing a phantom gel to thermally equilibrate at room temperature for at least 2 h before placing it into the bore of the magnet, with all other parameters fixed for the duration of the 30-min measurement. The random phase change observed was assumed to be the result of magnetic drifting, system vibration, and MRI system error.

3 Results

The temperature of each pixel in the thermal image maps was represented using a color-coded lookup table scheme.

Figure 2 shows the images of the real and imaginary parts of the data of a phantom gel after data reconstruction. In each graph, the laser beam was delivered to the center of the bottom surface of the sample. The phase mappings at 2.78 min and 12.66 min after laser irradiation, corresponding to temperature increases, are shown in Fig. 3. The area of the absorption-enhanced sphere with 0.25% ICG shows higher temperature increases.

The temporal profile of temperature distribution in a phantom gel is shown in Fig. 4. The sample was irradiated by the laser from the bottom. The ICG–enhanced area was near the bottom of the gel in this figure. The laser power was 1.0 W, with imaging dimensions of 128×128 pixels. The first image [Fig. 4(a)] was obtained 4.5 min after data collection (0.5 min before laser radiation). Figures 4(b)–4(k) show the

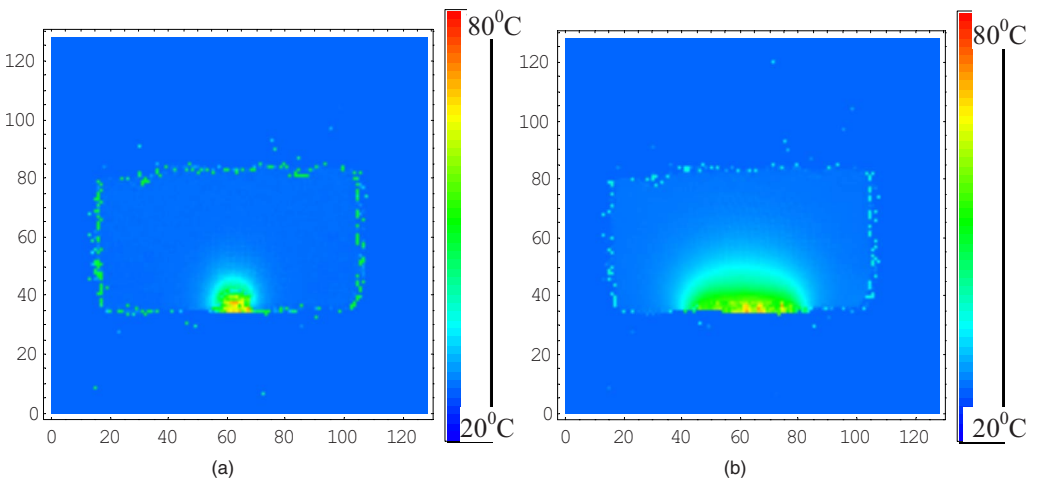

Fig. 3 Temperature distribution inside a phantom gel 2.78 min (a) and 12.66 min (b) after laser irradiation. The sample was irradiated from the bottom. The laser power density is 1.27 W/cm^2 with a laser power of 1.0 W. There is a phantom sphere (near the bottom of the sample) containing ICG (0.25%) embedded within the phantom gel to simulate the absorption-enhanced tumor.

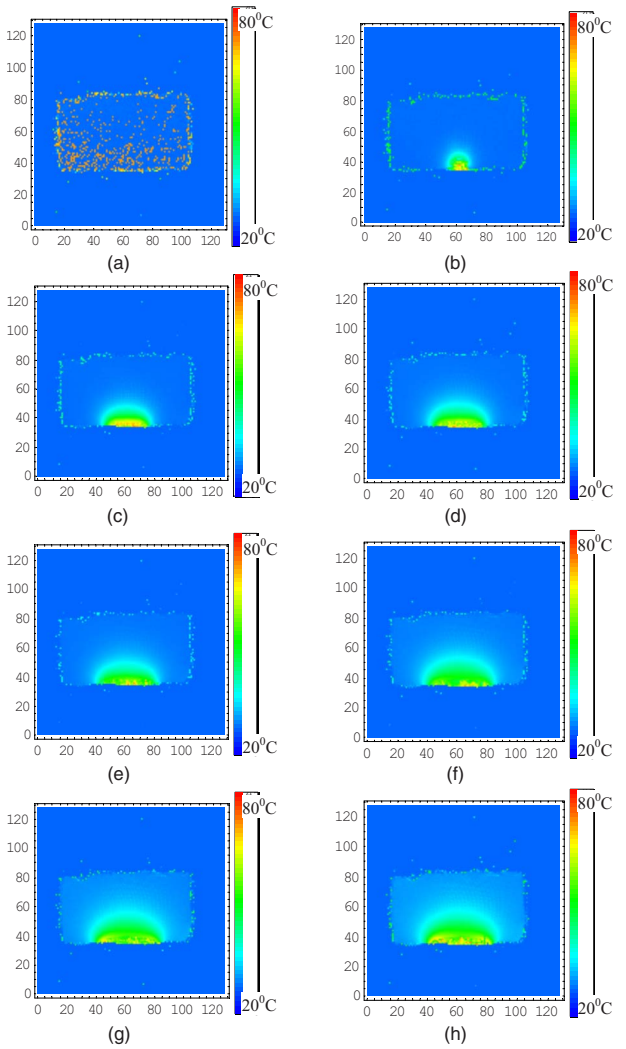

Fig. 4 Temporal profiles of temperature distribution in a phantom gel with imaging dimensions of 128×128 pixels. The laser power is 1.0 W (1.27 W/cm^2 power density). The sample was irradiated from the bottom. The first distribution (a) was acquired 4.5 min after the start of the MRI data collection (before laser irradiation). (b) to (h) Temperature distributions acquired from 7.8 min to 27.6 min, with a 3.3-min increment, after the start of the MRI data collection. The laser began 5 min after the start of the MRI data collection, with a 10-min duration. There is a phantom sphere (near the bottom of the sample) containing ICG (0.25%) embedded within the phantom gel to simulate the absorption-enhanced tumor.

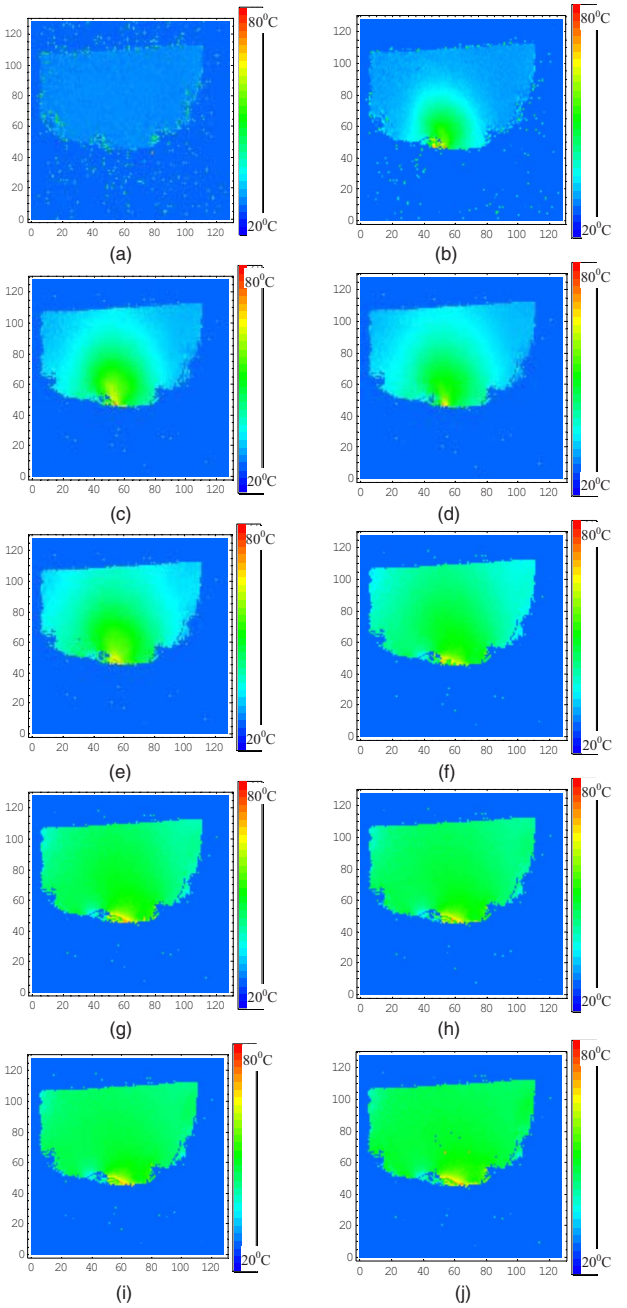

Fig. 5 Temporal profile of temperature distribution in chicken tissue with imaging dimensions of 128×128 pixels. The laser power is 3.0 W (power density of 1.17 W/cm^2 with a beam diameter of 1.8 cm). The sample was irradiated from the bottom. The first distribution (a) was acquired 4.5 min after the start of the MRI data collection (before laser irradiation). (b) to (j) Temperature distributions acquired from 7.5 min to 31.5 min, with a 3.3-min increment, after the start of the MRI data collection. The laser began 5 min after the start of the MRI data collection, with a 10-min duration.

temperature distributions in the samples measured from 7.8 min to 27.8 min after MRI data collection began, with a 3.3-min increment. The maximum temperature elevation was around 40 to 43°C in the center of the dye absorption–enhanced area, as shown in Fig. 4(e).

The temperature evolution of the chicken tissue is shown in Fig. 5. The laser power was 3.0 W, with imaging dimensions of 128×128. The power density was 1.17 W/cm^2 (beam diameter of 1.8 cm). The first image [Fig. 5(a)] was obtained 4.5 min after data collection, which was about 0.5 min before laser radiation. Figures 5(b)–5(k) show the temperature distributions in the chicken samples measured from 7.5 min to 31.5 min after MRI data collection, with a 3.0-min increment. The maximum temperature elevation was around 36 to 39°C, as shown in Figs. 5(d) and 5(e).

The initial temperature measurements were recorded, and calibration measurements were performed to determine the proton resonance shift coefficient and the system calibration factor. A series of calibrations using the natural temperature

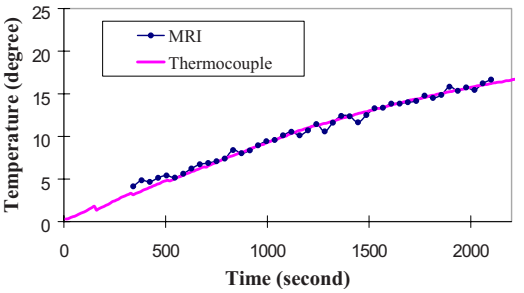

Fig. 6 Temperature calibration using MRI and a thermocouple for chicken breast tissue. The chicken tissue was placed in a refrigerator at 3°C and then placed in room temperature for 40 min. The temperature near the center (pixel [60, 60]) was measured both by MRT and by thermocouple under the same conditions. The temperature-dependent water proton chemical shift coefficient was determined as 0.0105×10^{-6}.

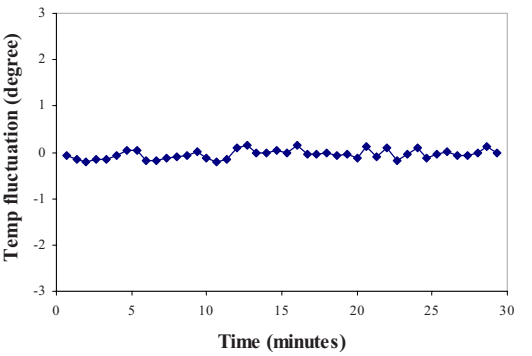

Fig. 8 System noise measurement. The temperature was measured under constant surrounding temperature and the same testing conditions. All the system noise is converted to the temperature fluctuation. The error of temperature measurement caused by this error factor is less than 0.4 deg.

elevation from nonequilibrium points (+2°C) to room temperature (+22°C) were performed using MRI thermal mapping. Figures 6 and 7 show the calibration using the phantom gel and chicken tissue with a natural temperature elevation from 2°C to 17°C. A thermocouple measurement was performed under the same conditions to obtain the temperature distribution at pixel position [60, 60] near the center of the sample for comparison with that of the MRI data. It was demonstrated that the MRI data were in good agreement with the thermocouple data after a system constant fitting. The temperature-dependent water proton chemical shift coefficient of the gelatin phantom gel was determined to be 0.0096 ppm. For the chicken data, the temperature-dependent water proton chemical shift coefficient was determined to be 0.0105 ppm, a 5% difference from the phantom gel measurement.[12]

For the resolution and stability evaluation, the temperature change was measured under the constant conditions described earlier. A phantom gel was stored at room temperature for at least 2 h prior to being placed into the bore of the magnet. With the sample at thermal equilibrium and all other environmental conditions remained the same, the temperature fluctuations were recorded over a period of 30 min. The acquired 45 phase images during this time provided a measure of MRI field drift as observed in the signal phase changes. From our measurements, the maximum temperature change was about 0.37°C, and the temperature standard deviation was 0.10°C (Fig. 8). If we assumed that all parameters were kept constant except for the fluctuation of B_0, the maximum drift of B_0 would be equal to 2.6×10^{-8} T. The corresponding temperature uncertainty was 0.37°C. This can be defined as the system resolution, since a temperature fluctuation less than 0.37°C will not be identified.

Rats were treated by the laser with a 2.55 W/cm^2 power density and a spot size of 1.0 cm diam. For each rat, except for the control rat, ICG solution (0.2 ml, 0.25%) was injected into the center of the tumor 20 min before laser treatment. The images obtained in the rats are shown in Figs. 9 and 10. The image at the 10-min point (at the end of the laser irradiation) had higher temperature elevation. This corresponds to a temperature of around 70 to 77°C (temperature elevation of 35 to 42°C). The maximum temperature increase was about 42°C at the top portion of the ICG-enhanced tumor (Figs. 9 and 10).

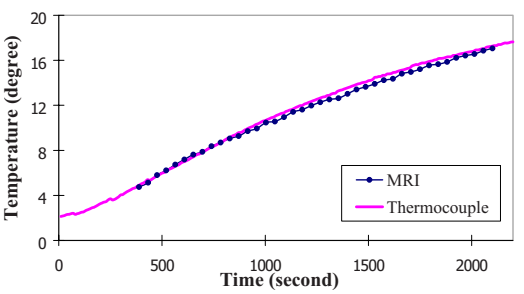

Fig. 7 Temperature calibration using MRI and a thermocouple for a phantom gel. The phantom gel had an initial temperature of 4.5°C and was placed in room temperature for 40 min. The temperature at pixel [60, 61] around the center of the gel was measured both by MRT and by thermocouple under the same conditions. The temperature-dependent water proton chemical shift coefficient was determined as 0.0096×10^{-6}.

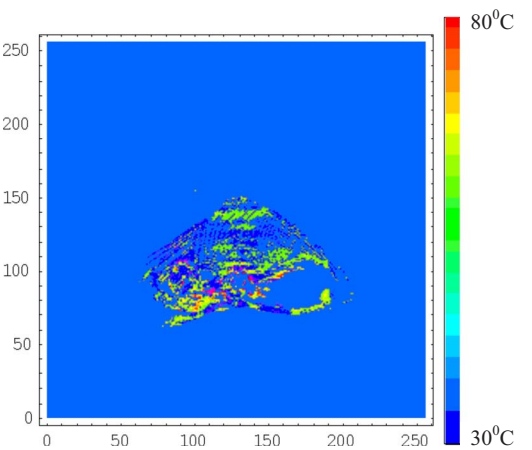

Fig. 9 Cross-sectional temperature distribution in a rat 2 min after laser irradiation. The laser beam was delivered from the top. The tumor was implanted on the back and covered by the skin. ICG solution (0.2 ml, 0.25%) was injected into the center of the tumor 20 min before laser treatment. The laser power density is 2.55 W/cm^2, with a beam size of 1.0 cm diameter.

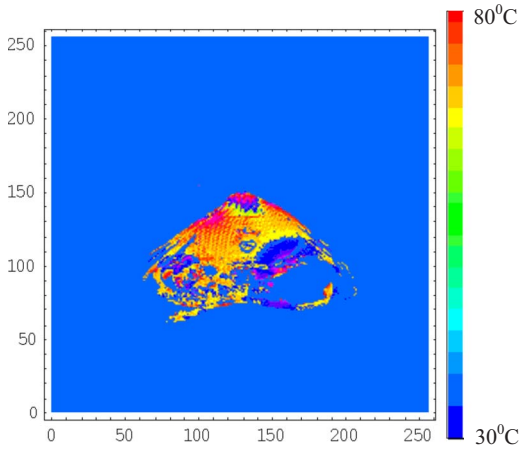

Fig. 10 Cross-sectional temperature distribution in a rat 10 min after laser irradiation. The laser beam was delivered from the top. The tumor was implanted on the back and covered by the skin. ICG solution (0.2 ml, 0.25%) was injected into the center of the tumor 20 min before laser treatment. The laser power density is 2.55 W/cm^2, with a beam size of 1.0 cm diameter.

4 Discussion

The purpose of our research is to find an *in vivo* temperature mapping for selective laser photothermal treatment. With accurate thermal information, we can find the correlation between the temperature and the immunological response for the tumor treatment. In the future, by using proper thermal dosage and duration, we can control the temperature elevation within tissue to optimize the selective photothermal cancer treatment.

Three-dimensional *in vivo* and *ex vitro* temperature distribution with high spatial resolution was obtained using MRI measurements based on the chemical shift of the water proton density resonance frequency (PRF). The PRF method is based on a simple gradient echo sequence (FLASH sequence) and has high signal-to-noise ratio and spatial resolution. It has advantages over other methods such as diffusion coefficient, which has low resolution along with high sensitivity to motion. The spatial resolution is in the range of 0.2 to 0.4 mm, with a slice thickness of 2.0 mm within the sample. Under normal laser thermotherapy conditions, the laser energy is delivered by optical fiber near the skin or incision. The temperature elevation is point-like, with a temperature difference of about 2 to 4 deg with spatial separation of 1 mm near the maximum temperature point. The fine spatial resolution is crucial for analyzing thermal effect and biological response under laser-tissue interaction. With the advances and accumulation of knowledge of tissue parameters, it is possible to obtain real-time, *in vivo* 3-D temperature profiles.

Motion-related error, random external field drift, phase-image noise, vibration, and varying temperature coefficients for different tissue components remain as potential sources of error. The magnetic field drift can cause phase change errors, which can reflect fictitious changes in temperature. Compared with other MRI thermometry methods such as the molecular diffusion coefficient of water, the PRF method has high resolution but is sensitive to the drift of the external magnetic field.[19] A simple computation shows that a 7×10^{-8} change in the magnetic field can result in a temperature measurement error on the order of 1.00°C. From our system evaluation, the total system error including magnetic field drift together with all other assumed possible system error yielded a temperature uncertainty of 0.100°C and a maximum fluctuation of 0.37°C. To this end, it is sufficient to assume a 0.40°C maximum system uncertainty as the system resolution.

Based on our system calibration, it was determined that the temperature-dependent water proton chemical shift coefficient was 1.05×10^{-2} ppm compared with the reported 1.0×10^{-2} ppm.[25] There is a possibility that the temperature monitored using a fiber sensor or thermocouple was not at the exact position measured using MRI. The disagreement of the PRF thermal coefficient was also reported by other researchers and may relate to the variations in the magnetic susceptibility of blood.[22] In our research, this indicates that the temperature coefficient can have a variance of about 5% between different tissues and gel samples. This may contribute to an absolute temperature error of approximately 1.5 to 2.0°C for temperature elevations in the range of 30 to 400°C. Such accuracy should be adequate for tissue temperature mapping to guide tumor treatment.

Tissue displacement has always been the problem for correctly identifying temperature elevation using phase mapping during laser thermometry. Normally, respiratory gating can be used to eliminate most of the displacement error. The structure changes and deformation of target tissue can be caused by thermal coagulation during the pulsed laser ablation.[26] We did not observe apparent displacement error except in the case of live animals without respiratory gating.

The spatial resolution of the chemical shift of the proton density method (~0.2 mm) makes it superior to other methods. Laser thermology requires high spatial resolution and fast data acquisition time because the thermal distribution changes rapidly with sharp thermal gradient within the tissue. In our experiments, each scan lasted about 45 s. The fast low-angle gradient echo sequences make fine temporal resolution possible. It should be pointed out that the spatial resolution is closely related with the total sampling time, which sets limits to the temporal resolution. We can obtain higher spatial resolution (for example, 256×256 pixels) with less slice division or by sacrificing temporal resolution.

The highest temperature elevation was reached near the surface under direct laser radiation. This temperature was higher than the normal tumor destruction temperature in the directly radiated surface area. Since not all the tumor area reached the maximum temperature, we hypothesize that not all tumor cells were destroyed. However, when laser irradiation was used in combination with immunological stimulation, such as the use of immunoadjuvant, a certain level of tumor cell destruction, although not complete destruction, may be sufficient to induce an immune response. Previous studies[7,9] strongly indicate the feasibility of a systemic effect by such combinations. Studies using MRI for tissue temperature determination could provide understanding and guidance to optimize the laser-induced, adjuvant-enhanced host immunity against residual local tumors and metastases at the distant sites.

ICG has been widely used for thermal enhancement in laser-induced heating.[27,28] In a recent study done by Yaseen et al.,[28] ICG is encapsulated with dextran polymer to avoid its

molecular instability and to increase biocompatibility and functionality. This shows a promising methodology for laser-induced therapy, especially in rapid circulation and molecular instability situations. In our research, which mainly focuses on the laser-induced immunological response for tumor treatment, direct tumor injection has the advantage of simplicity and a long ICG tissue retention time. Both studies show similar temperature elevation measured by thermocouple or MRI in the phantom gel under.

In summary, we demonstrated that the PRF method was an effective method for tissue temperature determination during noninvasive laser photothermal irradiation. Future experiments will focus on the selection of laser parameters and suitable dosages to achieve optimum immunological effects using laser immunotherapy under the guidance of magnetic resonance imaging.

Acknowledgments

This research was supported in part by grants from the University of Central Oklahoma and the National Institute of Health (Grant No. P20 RR016478 from the INBRE Program of the National Center for Research Resources).

References

1. W. R. Chen, W. G. Zhu, J. R. Dynlacht, H. Liu, and R. E. Nordquist, "Long-term tumor resistance induced by laser photoimmunotherapy," *Int. J. Cancer* **81**(5), 808–812 (1999).
2. P. Steiner, R. Botnar, S. N. Goldberg, G. S. Gazelle, and J. F. Debatin, "Monitoring of radio frequency tissue ablation in an interventional magnetic resonance environment. Preliminary *ex vivo* and *in vivo* results," *Invest. Radiol.* **32**(11), 671–678 (1997).
3. H. E. Cline, K. Hynynen, C. J. Hardy, R. D. Watkins, J. F. Schenck, and F. A. Jolesz, "MR temperature mapping of focused ultrasound surgery," *Magn. Reson. Med.* **31**(6), 628–636 (1994).
4. S. Levy, "Biophysical basis and cardiac lesions caused by different techniques of cardiac arrhythmia ablation," *Arch. Mal Coeur Vaiss* **88**(10), 1465–1469 (1995).
5. J. H. Kim and E. W. Hahn, "Clinical and biological studies of localized hyperthermia," *Cancer Res.* **39**(6), 2258–2261 (1979).
6. H. E. Cline, J. F. Schenck, R. D. Watkins, K. Hynynen, and F. A. Jolesz, "Magnetic resonance-guided thermal surgery," *Magn. Reson. Med.* **30**(1), 98–106 (1993).
7. W. R. Chen, A. K. Singhal, H. Liu, and R. E. Nordquist, "Antitumor immunity induced by laser immunotherapy and its adoptive transfer," *Cancer Res.* **61**(2), 459–461 (2001).
8. W. R. Chen, S. W. Jeong, M. D. Lucroy, R. F. Wolf, E. W. Howard, H. Liu, and R. E. Nordquist, "Induced anti-tumor immunity against DMBA-4 metastatic mammary tumors in rats using a novel approach," *Int. J. Cancer* **107**(6), 1053–1057 (2003).
9. W. R. Chen, J. W. Ritchey, K. E. Bartels, H. Liu, and R. E. Nordquist, "Effect of different components of laser immunotherapy in treatment of metastatic tumors in rats," *Cancer Res.* **62**(15), 4295–4299 (2002).
10. J. J. Crochet, S. C. Gnyawali, Y. Chen, E. C. Lemley, L. V. Wang, and W. R. Chen, "Temperature distribution in selective laser-tissue interaction," *J. Biomed. Opt.* **11**(3), 34031 (2006).
11. B. Quesson, J. A. Zwart, and C. T. Moonen, "Magnetic resonance temperature imaging for guidance of thermotherapy," *J. Magn. Reson Imaging* **12**, 525–533 (2000).
12. Y. Ishihara, A. Calderon, H. Watanabe, K. Okamoto, Y. Suzuki, K. Kuroda, and Y. Suzuki, "A precise and fast temperature mapping using water proton chemical shift," *Magn. Reson. Med.* **34**(6), 814–823 (1995).
13. H. E. Cline, K. Hynynen, E. Schneider, C. J. hardy, S. E. Maier, R. D. Watkins, and F. A. Jolesz, "Simultaneous magnetic resonance phase and magnitude temperature maps in muscle," *Magn. Reson. Med.* **35**, 309–315 (1996).
14. L. D. Hall and S. L. Talagala, "Mapping of pH and temperature distribution using chemical-shift-resolved tomography," *J. Magn. Reson. (1969-1992)* **65**, 501–505 (1985).
15. P. M. Jacob, C. Hendrich, T. Breitling, A. Schafer, A. Berden, and A. Haase, "Real time monitoring of laser-induced thermal changes in cartilage *in vitro* by using snapshot FLASH," *Magn. Reson. Med.* **37**, 805–808 (1997).
16. J. Olsrud, R. Wirstam, S. Brockstedt, A. M. Nilsson, K. Tranberg, F. Stahlberg, and B. R. Persson, "MRI thermometry in phantoms by use of the proton resonance frequency shift method: application to interstitial laser thermotherapy," *Phys. Med. Biol.* **43**, 2597–2613 (1998).
17. J. C. Hindman, "Proton resonance shift of water in the gas and liquid states," *J. Chem. Phys.* **44**(12), 4582–92 (1966).
18. W. G. Schneider, H. J. Bernstein, and J. A. Pople, "Proton magnetic resonance chemical shift of free (gaseous) and associated (liquid) hydride molecules," *J. Chem. Phys.* **28**(4), 601–607 (1958).
19. J. D. Poorter, C. D. Wagter, Y. D. Deene, C. Thomsen, F. Stahlberg, and E. Achten, "The proton resonance frequency-shift method compared with molecular diffusion for quantitative measurement of two-dimensional time-dependent temperature distribution in a phantom," *J. Magn. Reson.* **103**, 234–41 (1994).
20. T. Harth, T. Kahn, M. Rassek, B. Schwabe, H. J. Schwarzmaier, J. S. Lewin, and U. Modder, "Determination of laser-induced temperature distributions using echo shifted turbo FLASH," *Magn. Reson. Med.* **38**, 238–245 (1997).
21. N. Muller and R. C. Reiter, "Temperature dependence of chemical shifts of protons in hydrogen bonds," *J. Chem. Phys.* **42**(9), 3265–3269. (1965).
22. R. D. Peters, R. S. Hinks, and R. M. Henkelman, "*Ex vivo* tissue type independence in proton-resonance frequency shift MR thermometry," *Magn. Reson. Med.* **40**(3), 454–459 (1998).
23. R. Salomir, J. Palussiere, N. Grenier, E. Dumont, B. Quesson, and C. Moonen, "Local hyperthermia with focused ultrasound (FUS) or interstitial laser applicator (LITT) under PRF-based MR-temperature monitoring in the living kidney of the rabbit," in *Proc. 10th Annual Meeting of ISMRM*, Honolulu, pp. 2202 (2002).
24. S. Morikawa, T. Inubushi, Y. Kurumi, S. Naka, V. Seshan, and T. Tsukamoto, "Feasibility of simple respiratory triggering in MR-guided interventional procedures for liver tumors under general anesthesia," in *Proc. 10th Annual Meeting of ISMRM*, Honolulu, pp. 2240 (2002).
25. F. Bertsch, J. Mattner, M. K. Stehling, U. Muller-Lisse, M. Peller, R. Loeffler, J. Weber, K. Mebmer, W. Wilmanns, R. Issels, and M. Reiser, "Noninvasive temperature mapping using MRI: comparison of two methods based on chemical shift and T_1-relaxation," *Magn. Reson. Med.* **16**(4), 393–404 (1998).
26. V. Rieke, K. K. Vigen, G. Sommer, B. L. Daniel, J. M. Pauly, and K. Butts, "Referenceless PRF shift thermometry," *Magn. Reson. Med.* **51**, 1223–1231 (2004).
27. W. R. Chen, R. L. Adams, S. Heaton, D. T. Dickey, K. E. Bartels, and R. E. Nordquist, "Chromophore-enhanced laser tumor tissue photothermal interaction using an 808-nm diode laser," *Cancer Lett.* **88**, 15–19 (1995).
28. M. A. Yaseen, J. Yu, M. S. Wong, and B. Anvari, "Laser-induced heating of dextran-coated mesocapsules containing indocyanine green," Biotechnol. Prog. ASAP Article (2007).